CORRELATING LARGE SETS OF EXPERIMENTAL DATA WITH HIGH RESOLUTION COMPUTATIONAL WELD MECHANICS MODELS

J. GOLDAK*, M. MARTINEZ**, S. TCHERNOV*, H. NIMROUZI*, J. ZHOU*, D. K. AIDUN** and H. EISAZADEH***

*Goldak Technologies Inc., 3745 Revelstoke Dr., Ottawa, ON, K1V 7C2, Canada.
**Clarkson University, Department of Mechanical and Aeronautical Engineering, 8 Clarkson Av, Potsdam, NY, 13699, USA., mmartine@clarkson.edu
***Mechanical Engineering Technology, Old Dominion University, 108B Kaufman Hall, Norfolk, VA 23529, USA

DOI 10.3217/978-3-85125-615-4-43

ABSTRACT

The validity of 3D transient computer models to predict the mechanics of welds is judged by correlating predictions made by the computer model with data acquired from experiments, i.e., correlating virtual and real data. The authors suspect that by far the greatest uncertainty in the predictions from these computational models has been due to the sparsity in the available experimental data on material properties and the welding process itself. The goal of this paper is to present a few examples that demonstrate how large sets of experimental data provided by recent developments in sensor technology and data acquisition systems such as distributed fiber optic temperature and strain sensing optical fiber, in addition to full field and transient data such as thermographic and Digital Image Correlation (DIC) cameras can be correlated with predictions from VrWeld, a computer model for computational weld mechanics. A fiber optic system using Rayleigh backscattering is used to measure temperature and strain with a spatial resolution of 0.65 mm at a data acquisition rate of 10 Hz but it could be as high as 250 Hz. The experimental data has noise that must be filtered. To correlate the virtual data the 3D transient Computational Weld Mechanics (CWM) models had to use time steps smaller than 1 second and element size less than 1 mm. With this data, one can correlate the clocks for the experiment and the computer model. In addition, one can run Design of Experiments (DOEs) to correlate material properties such as temperature dependent thermal conductivity and boundary conditions such as convection coefficients. Some of the challenges in synchronizing real and virtual data in space and time are discussed.

Keywords: Transient Welding Analysis, Digital Image Correlation, Thermography of Welds, Computational Welding Models.

INTRODUCTION

The objective of this study was to provide an example of the correlation between modern experimental methods and a current computer model of welds, i.e., to estimate the

uncertainty in the validation of one particular current computer model - VrWeld. The approach is to correlate as much experimental data, particularly transient, full field experimental data, as we can afford to collect with as much 3D transient full field virtual data as we can afford to compute. We do not seek the value of a binary decision of whether the computer model is valid or not valid. Rather we seek measures of the correlation between each type of real and virtual data. Because the physical and virtual experiments use different clocks and different coordinate frames, one of the first challenges is to synchronize the physical and virtual clocks and physical and virtual spatial coordinate frames.

DESIGN OF THE EXPERIMENT

Our study is divided into five sections: (i) a description of a 3D transient computer weld model; (ii) a detailed explanation on the synchronization of the clock data for different experimental data sets and the computer model; (iii) an optimization Design of Experiment (DOE) study to compute estimates of the sensitivity of parameters in the computational model; (iv) a transient analysis result section which discusses the correlation of real and virtual DIC data; (v) a discussion and conclusion section.

Our study made use of an A36 300 × 300 × 6.35 mm steel plate. A 90-degree V-groove weld joint runs the length of the plate on the symmetry plane. The welding process was a manual GTAW with 1/16-inch ER 70S2 filler metal added. The arc was 180 amps and 15 volts. A 50/50 mixture of argon and helium shielding gas at 30 CFM was used. The plate was fixed in the vertical plane. The weld was made upward (3G position). The weld length was 270 mm; the total time for the weld was 280 seconds. Data was gathered for a total time of 30 minutes from the start of welding in order to capture the behavior during cool-down after the weld was complete.

Fig. 1 shows the setup used for this study. As seen in this figure the front of the plate was instrumented with a fiber optic sensor connected to a Rayleigh backscattering system from Luna Technologies [1]. Also seen in the test setup, the back of the plate was painted with very high temperature paint with a speckle pattern which allowed for acquisition of the strain distribution in situ during the welding process using a VIC-3D Digital Image Correlation System [2]. A fan was also placed blowing room temperature air towards the back of the plate. This was required in order to avoid heat buildup in the air between the plate and the camera. Furthermore, the plate was clamped to a portrait fixture which allowed the authors to rotate the specimen to specific orientation. In this study the plate was set to approximately 90 degrees from the base of the table.

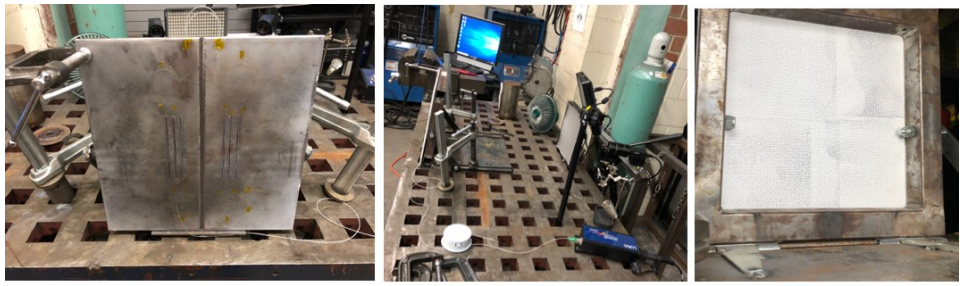

Fig. 1 Experimental Setup.

TRANSIENT 3D COMPUTER MODEL OF WELD

The weld heat source model is based on models proposed by Ohji et al. [3] and Sudnik [4]. The weld heat source model is a 3D transient Eulerian formulation that solves the conservation of energy, mass and momentum with a Gaussian pressure distribution, thermal flux distribution and mass flux distribution from the arc. The effects of surface tension and gravity were included. Patterns for weave welds with weave amplitude and dwell times are supported in the model. Melting, solidification and the evolution of microstructure were modelled. This heat source model predicts the weld shape and size. This is in sharp contrast to the distributed power density that is often called the double ellipsoid heat source model that requires the weld pool shape and size be known experimentally [5].

The conservation of energy in spatial coordinates is solved using a semi-Lagrange method:

$$\rho \frac{dh}{dt} - \nabla \cdot \mathrm{q} + \mathrm{Q} = 0 \tag{1}$$

Where, ρ is density, h is specific enthalpy, q is theral flux and Q is power per unit volume. The specific heat and thermal conductivity are functions of temperature and phase fractions. The transient transformations of austenite to ferrite, pearlite, bainite and martensite and the grain growth of austenite were computed in the model.

The quasi-static conservation of momentum in spatial coordinates was solved using a semi- Lagrange method.

$$\nabla \cdot \sigma + g = 0 \tag{2}$$

and

$$\Delta \mathrm{p} = \gamma \left(\frac{1}{R_1} + \frac{1}{R_2} \right) \tag{3}$$

Where, σ is the Cauchy stress, g is the acceleration due to gravity, Δp is the pressure drop across the liquid-plasma interface, γ is the surface tension and $1/R_1$, $1/R_2$ are the

principal curvatures at a point on the liquid surface. The inertial force and Marangoni forces are neglected in this model.

The conservation of mass is enforced as a constraint such that the mass flow in the wire, $\pi r_{wire}^2 v_{wire} = A_{filler} v_{weld}$ where r_{wire} is the radius of the wire, v_{wire} is the wire speed, v_{weld} is the weld speed and A_{filler} is the cross-sectional area of the filler metal. Weld pool model requires all parameters of most weld procedures plus additional parameters such as surface tension and arc pressure that are not usually included in weld procedure data sheet.

INPUTS TO THE VRWELD MODEL

The VrWeld heat source model required input of the power needed to perform the weld. Thus, the video captured during the actual weld process of the welding station which displayed the instantaneous voltage and current was transformed into a graph of current and voltage vs. time as shown in Fig. 2.

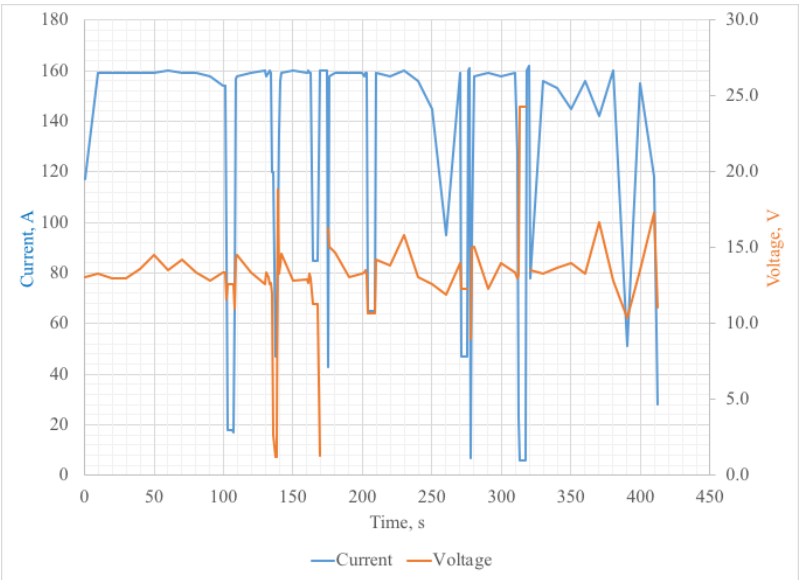

Fig. 2 Voltage and Current vs. Time during the welding process.

The power input causes burn-through on the backside of the plate. Fig. 3, relates the virtual burn-through and the real burn-through shown. The width of the virtual burn-through in the left image and the width of the real burn-through in the photograph on the right are both close to 8 mm. This comparison is indicative that weld pool model parameters have generated a weld pool shape that agrees well with the observed data. This real data is very important because it provides a constraint that the weld pool model design parameters must satisfy.

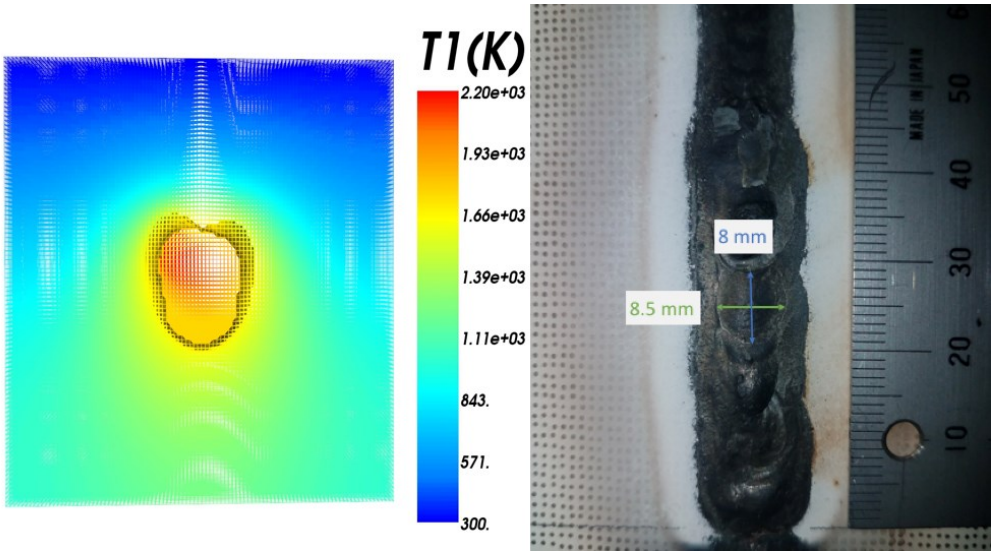

Fig. 3 The left image shows iso-surfaces of the temperature 5 degrees above and below the melting point on the bottom surface at time 45 seconds. The right image shows the burn through on the bottom of the plate after the weld had cooled. Both predicted and measured burn-through are approximately 8.5 mm.

In addition, the burn-through, the VrWeld model accounts for the weaving motion performed by the welder during the welding process. This is an important input parameter in the model due to the manual nature of the welding process being considered in this study. Fig. 4 shows some of the results of the VrWeld model, each row of images has one image with a left weave and a right weave. The top row is 6 seconds after the start of the weld. The second row is about 15 seconds after the weld started, while the last row is approximately 45 seconds after the weld started. If computer vision data was available, it would provide a strong constraint that the design parameters the weld pool model should satisfy, e.g., arc pressure distribution and surface tension. The weld pool model used a Gaussian arc pressure distribution with parameters for the integral and width of the Gaussian function.

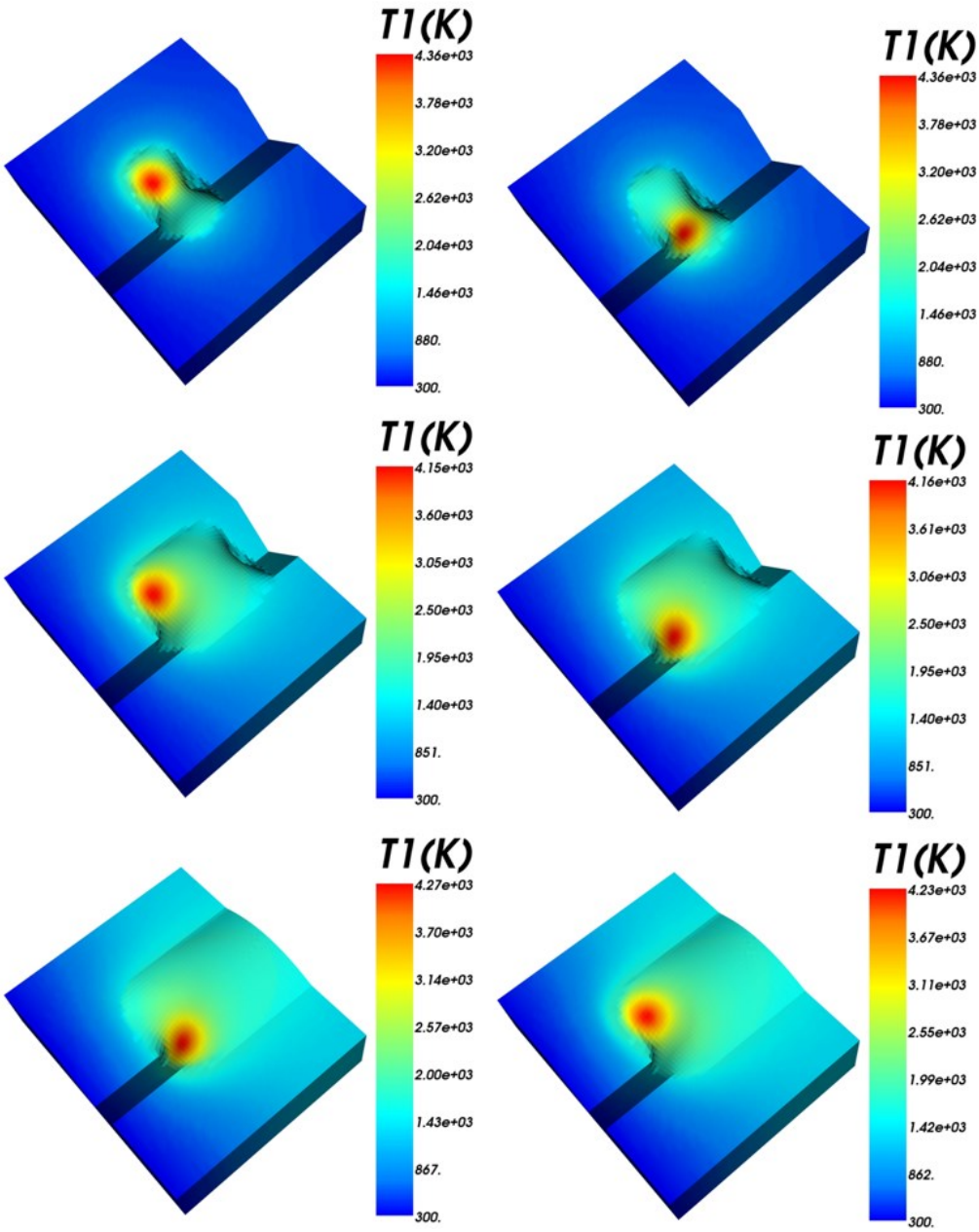

Fig. 4 The image of the weld pool surface is shown for a sequence of time steps. The color represents the temperature in °K.

PHASE TRANSFORMATION

An important outcome of the VrWeld model is the coupling of the temperature fields to material phase transformation models. Fig. 5 shows the isosurfaces for the temperature 5°K below the melting temperature in blue and 5°K above the melting point in red. The region between the isosurfaces in front of the weld pool is melting. The region between the isosurfaces behind the weld pool is solidifying.

In Fig. 6, the top right image shows isosurfaces for phase fraction austenite of 0.05 and 0.95. The region between the outer two isosurfaces shows where fraction of austenite and ferrite-pearlite is increasing or decreasing. The region between the inner two isosurfaces is where austenite and liquid phases are increasing or decreasing. These images are at time 14 and 14.5 seconds after the start of the weld, respectively. We have ignored the delta ferrite phase in this model.

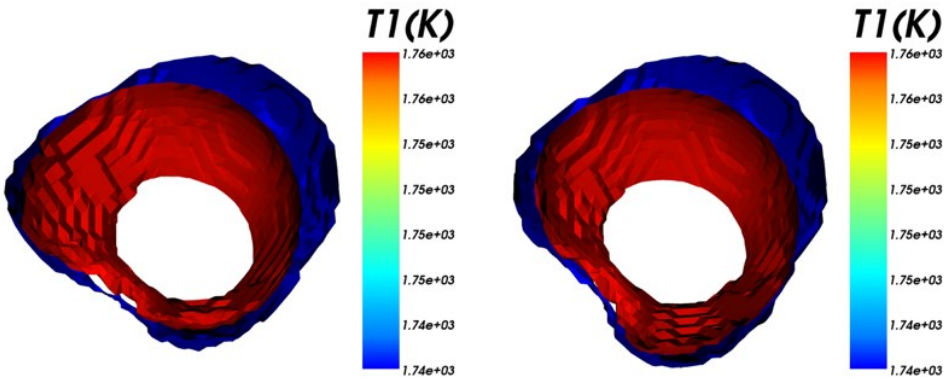

Fig. 5: The top left image shows the isotherms for temperatures 10 °K above and below the melting temperature.

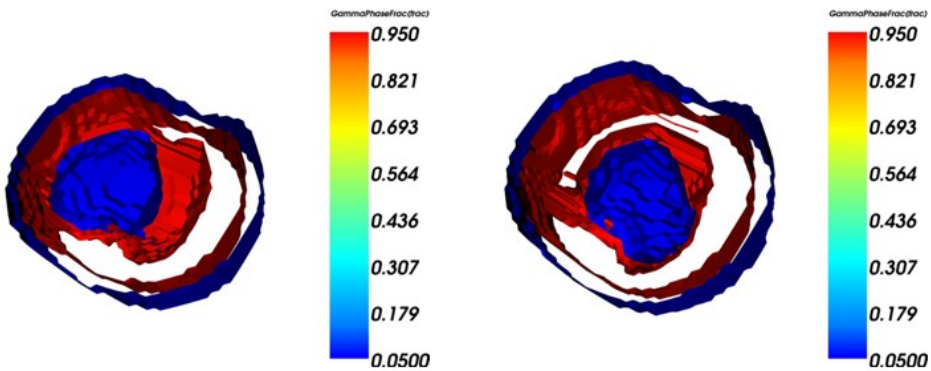

Fig. 6: Iso-Surfaces of the 0.05 and 0.95 fraction of the austenite phase are shown at time 14 seconds in the left image and 14.5 seconds in the right image

Fig. 7 shows virtual temperature data, however it is important to note that this data has not yet been correlated to real temperature data.

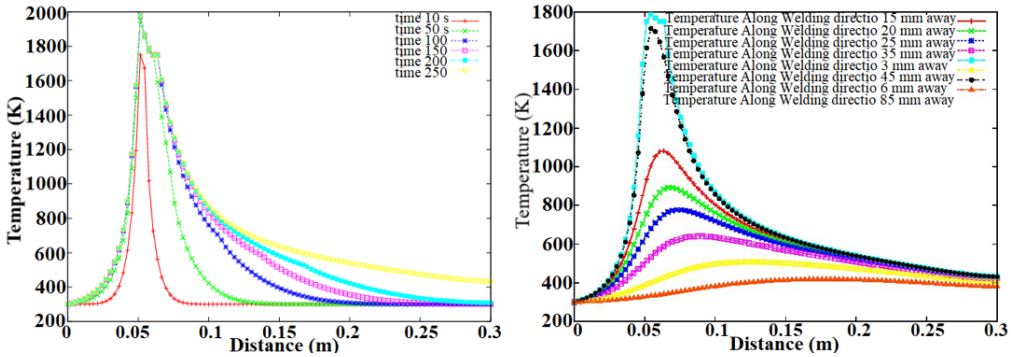

Fig. 7 The left image shows plots of the virtual temperature on the weld path line on the bottom surface for a sequence of time steps in the weld. The right image shows virtual temperatures at an instant of time on lines on the bottom surface of the plate at increasing distances from the weld path.

Fig. 7 shows the temperature profile along the weld line, while the same figure on the right shows the temperature profiles on the bottom or back surface offset from the weld line. As shown in Fig. 7, the approximate zero slopes near the peak are the mushy zone for melting in front of and for solidification behind the weld pool. These straight sections at the high temperature values for the two plot is due to the phase changes. During the phase change the enthalpy changes however temperature is kept constant. The right image shows plots of the virtual temperature at an instant of time on lines parallel to the weld path line at different transverse distances from the weld path. Note that the high frequency temperature oscillations near the 1800°K peak that are thought to be due to weaving. Note that the oscillations decay with distance from the weld and cannot be seen in line plots with lower peak temperatures that are farther from the weld path.

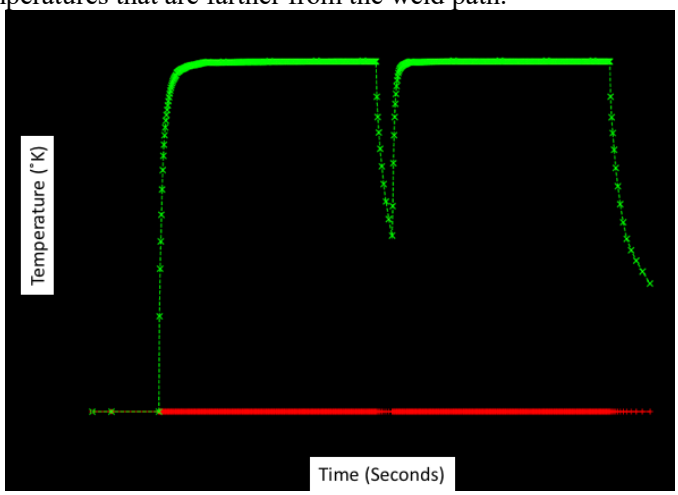

Fig. 8 The minimum and maximum temperatures in each time step in the virtual analysis.

Note the decay in maximum temperature near 200 seconds shown in Fig. 8. It corresponds to the time when the welder stops welding to change his filler metal wire.

SYNCHRONIZING CLOCKS FOR REAL AND VIRTUAL THERMAL DATA

The first virtual analysis was run with values of parameters claimed to be correct for the real welding experiment. The four sensor systems; DIC, Voltage-current, Fiber optic and FLIR Thermographic data acquisition systems, have independent clocks. The virtual model must synchronize the virtual clock with the four real clocks. We first assume that each of these clocks keeps perfect time in the sense that they would each measure the length of one hour exactly. Then N-1 offset times are computed to synchronize the N clocks.

Clocks for real and virtual thermocouples with similar locations in the real and virtual plate can be synchronized by correlating peak times for thermocouples with similar locations in the real and virtual plate. The time a thermal sensor detects peak temperatures for a given weld pass depends on its position with respect to the weld path. A local coordinate system is defined such that *w* is the distance along the weld path, *u* is the distance in the plane of the plate transverse to the weld path, and the *v*-coordinate is the distance through the thickness of the plate. The clock for the data acquisition instruments is started a few seconds before the arc is struck. As the arc travels along the weld path, heat diffuses transverse to the arc. The time to diffuse from the weld pool to the thermal sensor is sensitive to the (u,v,w) coordinates of the real and virtual temperature sensor.

In order to correlate the peak times of each real and virtual thermal sensor, Eq. 4 is solved for the following regression:

$$\begin{bmatrix} 1 & w_1 & u_1 & w_1^2 & w_1 d_1 & d_1^2 \\ 1 & w_2 & u_2 & w_2^2 & w_2 d_2 & d_2^2 \\ \vdots & \vdots & \vdots & \vdots & \vdots & \vdots \\ 1 & w_n & u_n & w_n^2 & w_n d_n & d_n^2 \end{bmatrix} \begin{bmatrix} a_0 \\ a_1 \\ \vdots \\ a_6 \end{bmatrix} = \begin{bmatrix} \Delta t_1 \\ \Delta t_2 \\ \vdots \\ \Delta t_n \end{bmatrix} \tag{4}$$

The matrix for the least square problem has one row for each thermal sensor that has the values (1, *w, d, w*^{2}*, wd, d*^{2}) where (*w, d*) are the coordinates of the thermal sensor where *w* is the distance along weld path from the weld path start point and *d* is the distance from the weld path for this thermocouple (TC). The real and virtual sensors are assumed to have the same (u,v,w) coordinates. This is an assumption that the location of the real sensor is known exactly. The n^{th} component of the right hand side vector has the value of the difference in the peak times for the n^{th} real and virtual thermal sensor located at (u_n,v_n,w_n).

In addition, (u_i,w_i) are the (u,w) coordinates of the i^{th} thermal sensor. The parameter a_0 is a measure of the average difference in the time between the real and virtual sensor reaches its peak temperature. While, the parameter a_1 is a measure of the difference in the time that each pair of real and virtual thermal sensors reaches their peak temperatures as a function of distance parallel to the weld path. The parameter a_2 is a measure of the difference in the time that each thermal sensor reaches its peak temperature as a function of distance normal to the weld path. Δt_n is the difference in time that real and virtual thermal sensor pair n located at (u_n,v_n,w_n) reach their peak temperatures.

DESIGN OF EXPERIMENT TO OPTIMIZE PARAMETERS IN THE COMPUTER MODEL

The first virtual model is idealized to model parameters of a constant speed, constant weld power with constant weave pattern. This idealization is not imposed by the computer model, it is imposed by the limitations of the information provided before correlating virtual data with data obtained from the sensors in the real experiment.

If the clocks and spatial coordinate frames were perfectly synchronized and if the virtual experiment perfectly replicated the real experiment, the difference in peak times would be zero. The first goal was to compute the start time for the virtual clock that minimizes the sum of squares of the difference in peak times of the pairs of real and virtual sensors $\sum_{i=1}^{n} \Delta t_i^2$. This was done shifting the start time of the virtual clock using the regression analysis shown in Eq. 4.

This correlation is done by running a Design of Experiment (DOE) analysis to minimize an objective function with a Design Matrix. Each design variable is one column in the DOE matrix and each row of the DOE matrix is one virtual experiment. One could also run multiple real and virtual experiments that solves the 3D transient weld pool model and 3D transient thermal analysis, where each row corresponds to an associated pair of a real and virtual experiments. Each design variable can have a specified lower bound, upper bound, minimum and maximum increment and a proposed initial guess.

The DOE matrix has one column for each design variable and one row for each numerical experiment. To optimize the weld speed, the DOE matrix has one design variable, the weld speed. The DOE matrix specifies an upper bound and a lower bound for each design variable. The usual objective function is to minimize the sum of squares of differences between real and virtual observables variables that are usually called design variables. To optimize virtual weld speed, the objective function minimizes a sum of squares of the difference in peak times of the real and virtual sensor $\sum_{i=1}^{n} \Delta t_i^2$, i.e., the weld speed that minimizes this objective function is computed.

A stochastic analysis with a kriging algorithm [6] is then used to compute a surrogate model for the design space for the virtual trials that have been completed. The number of virtual experiments to be run in each sub-set of trials is specified. If the number of trial sets has not reached its specified limit and if the allowed resources such as computing time have not been exceeded, a new set of virtual trials will be run until the limit is reached. This surrogate model contains estimates of the optimal value of each virtual design variable to minimize the sum of squares of differences between real and virtual observables or design variables. It can also evaluate the sensitivity of each design with respect to the objective function.

The second goal was to compute a virtual weld speed to minimize the difference in peak times. In the early stages of correlating real and virtual data, the virtual weld model uses a constant weld speed that is viewed as the average weld speed. Of course, this is an approximation as the speed of a manual weld is not really constant as the welder moves the

electrode to control the weld pool. If the virtual weld speed is slower than the average real weld speed, then virtual peak times for thermal sensor data near the start of the weld will be earlier than the peak times for the real thermal sensors, and peak times for thermal sensors near the end of the weld will be later than the peak times for the real thermal sensors. This assumes the weld speed is constant. In this case the real thermal sensor data was captured using the distributed fiber optic sensor. This system allows for capturing temperature data every 0.65 mm along the fiber length, thus creating an array of thermocouples longitudinal to the weld path.

If the weld speed varied as a function of time, as it does in manual welds, it would be desirable to include such variations in the analysis. Much of the difference is thought to be because of differences between the real and virtual local weld speed and local weld power as shown in Fig. 9. It is important to note that this figure correlates real and virtual data.

To optimize the virtual weld speed, a kriging analysis was run in which the objective function minimizes the sum of squares of the difference in peak times of the real and virtual sensor $\sum_{i=1}^{n} \Delta t_i^2$.

After the virtual clock and the real clock have been synchronized and differences in weld speed have been minimized, the values in the parameters for the virtual weld power, and convection coefficient are optimized. This is done by minimizing differences in the shape of the temperature peak for each pair of real and virtual thermal sensors. The convection coefficient and ambient temperature is most sensitive to thermal sensors far from the weld pool and during cool-down after the weld has been completed. The temperature peaks in sensors near the weld are sensitive to weld power distribution and to errors in the location of the thermal sensors and the lateral position of the weld pool as a function of time. If the temperature gradient at time *t* at a thermal sensor is 100 degrees per mm, then an error in position of 1 mm could generate an error in temperature of 100 degrees at time *t*.

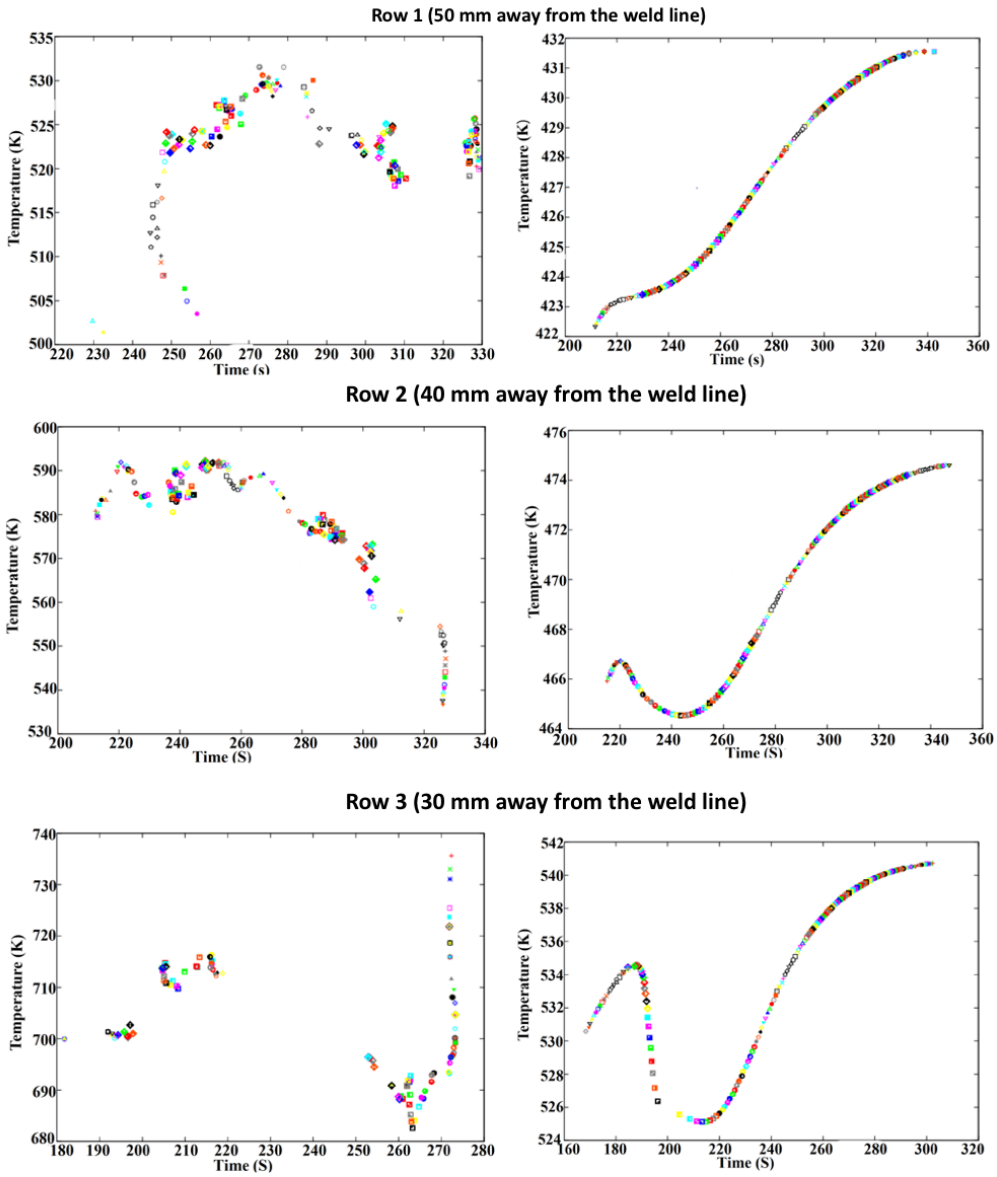

Fig. 9 The left images shows the real peak temperatures for the fiber data at 50, 40 and 30 mm from the weld path. The right images show the corresponding virtual peak temperatures.

In addition to the fiber optic senor data, a FLIR One Pro thermographic camera was used in this study. The real and virtual isotherms for temperatures of 100, 200, 300 and 400°C are computed. The difference in the area of each real and virtual isotherm at each discrete time step was calculated as shown in Fig. 10.

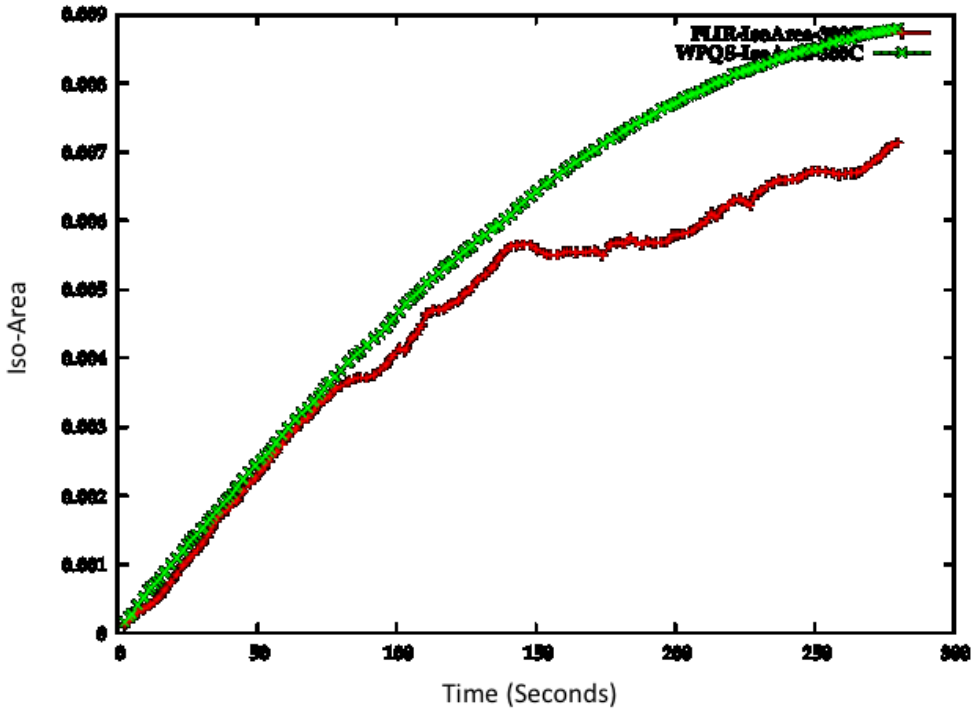

Fig. 10 The red curve is the area in units of m^2 of the 300°C isotherm computed from the thermographic data vs time. The green curve shows the area of the 300 °C isotherm vs time computed by VrWeld. The x-axis shows time in seconds.

As seen in Fig. 10, after 75 seconds the VrWeld model and real data deviate, this suggests that the power distribution or the power in the real weld was reduced in the last half of the weld. This figure correlates real thermographic data with virtual thermographic data from the VrWeld model.

Fig. 11, shows the actual comparison at one of the time steps between the VrWeld model and those captured by the FLIR One Pro thermographic data. These images have different camera positions and the perspectives are different. The difference in the shapes of the tails of the isotherm presents an opportunity to study why they differ. Possible causes may include differences in microstructure, phase transformations and differences in material properties of the filler metal and base metal.

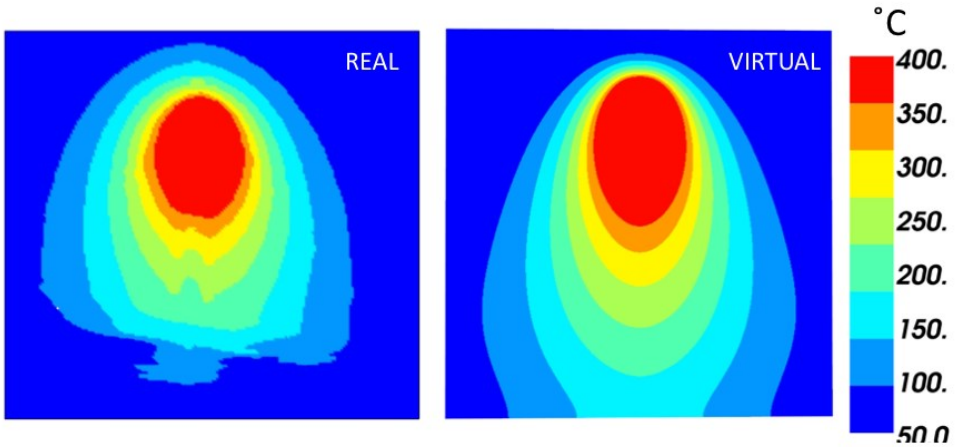

Fig. 11 The left image shows isotherms captured by the thermographic camera at 45 seconds The right image shows virtual isotherms computed by VrWeld at 45 seconds.

As seen in Fig. 12, the red curve in the right image shows the derivative of the curve in the left image with respect to time. The green curve is the red curve filtered to reduce high frequency fluctuations. The green curve is an estimate of the weld speed as a function of time in units of m/s. As such the right image provides the instanteneous weld speed, the green curve shows the smoothed curve. Based on the results obtained from the thermography data shown in Fig. 12, an average of 0.5 mm/s weld speed was estimated.

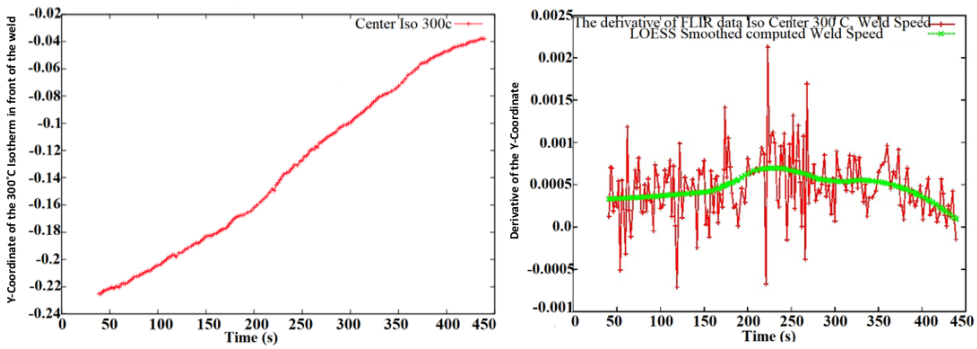

Fig. 12 The left image shows the longitudinal or y-coordinate of the 300 °C isotherm captured by the thermographic camera as a function of time. The right picture shows the derivative of the left picture with respect to the time. The red curve is raw values of the derivative. The green curve shows filltered data.

TRANSIENT THERMAL STRESS ANALYSIS

Digital Image Correlation (DIC) is an experimental technique used to measure transient displacement or deformation fields. From the measured displacement fields, strain fields can be computed. In contrast, FEM computes a strain field based on displacements computed by a computer model. The essential difference between DIC and FEM is DIC

measures a displacement field by using stereo cameras to measure the deformation of a speckle pattern while FEM solves integral equations to compute the transient displacement in a mesh.

One of the drawbacks with DIC, is its inability to correlate displacement close to the weld pool. We set DIC values to zero at points for which the DIC cannot correlate the deformation of the speckle pattern. We use this as a surrogate transient fiducial mark to correlate real and virtual displacements as described in Fig. 13.

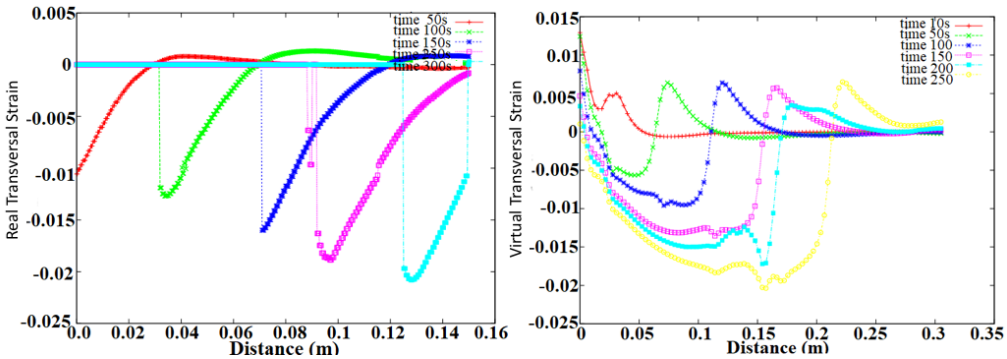

Fig. 13 The left image shows line plots from DIC data for transverse strain at five different times during the weld. The lines are parallel to the weld joint on the bottom surface of the plate. The lines for DIC data ends when the real deformation exceeds the DIC software's capability to correlate image data. The right image shows the corresponding line plots for the virtual DIC data.

As observed in Fig. 13, due to the inability of the DIC to cross correlate the strain near the passing of the weld pool, the values of strain are set to zero. As such the comparison between the virtual and DIC strain should be focused solely on the peaks and the decay away from the weld pool. Fig. 13 on the right is taken from the virtual DIC data set, as such the VrWeld allows for the computation of the strain along all locations of the finite element mesh.

WELD INTERRUPTION FOR FILLER ROD EXCHANGE

Fig. 14 and Fig.15, show the transversal and longitudinal strains captured by the DIC system during the interruption of the weld in order to perform an exchange of the filler rod. As seen in these two figures a complex formation of both transversal and longitudinal strains develops during this process as described next:

- Immediately prior to extinguishing the weld arc. The transversal strain (Fig. 14) above the liquid weld pool is found to be -13,599 με in compression, while on the left (west) side of the weld pool it is +8,918 με. This combination of strains indicates the pry open nature of the weld pool on the material as its being welded. The compressive region on top of the weld pool is caused by the tensile strain on

the side of the weld pool. The longitudinal strain readings at the same locations (Fig. 15) with respect to the welding pool are +3,488 με and +5,029 με in tension.

- When the arc is switched off, a cooling of the weld pool initiates immediately followed by a solidification on the back side as captured by the DIC cameras. Transversal strain (Fig. 14) readings drop to -15,352 με in the compression region just in front of the weld pool followed by a tensile region reaching +874 με further up on the plate. In contrast, the longitudinal strain (Fig. 15) right above the weld pool is in the order +4,794 με in tension.

- Liquid weld pool solidifies on the back side. Transversal compressive region (Fig. 14) becomes more compressed (strain value of -16,771 με) while the longitudinal strain at the same location is measured to be +5,493 με (Fig. 15).

- Weld arc is back on, the material is liquefied. The strain in transversal compressive region drops further to -19,457 με while in the tensile region above drops to +128 με (Fig. 14). Longitudinal strain above weld pool +6,652 με (Fig. 15).

It is interesting to see through this process how the exchange of a filler rod increases the local compressive transversal strain by almost -5858 με in front of the weld pool. It is also important to note that the vertical nature of the weld causes an increase in this compressive local transversal strain from the beginning to the end of the weld. The longitudinal local strain in front of the local weld pool also suffers an increase of approximately 3164 με in tension due to the filler rod exchange. This is a significant increase in both transversal and longitudinal strain near the weld pool every time the welder is required to exchange the filler rod.

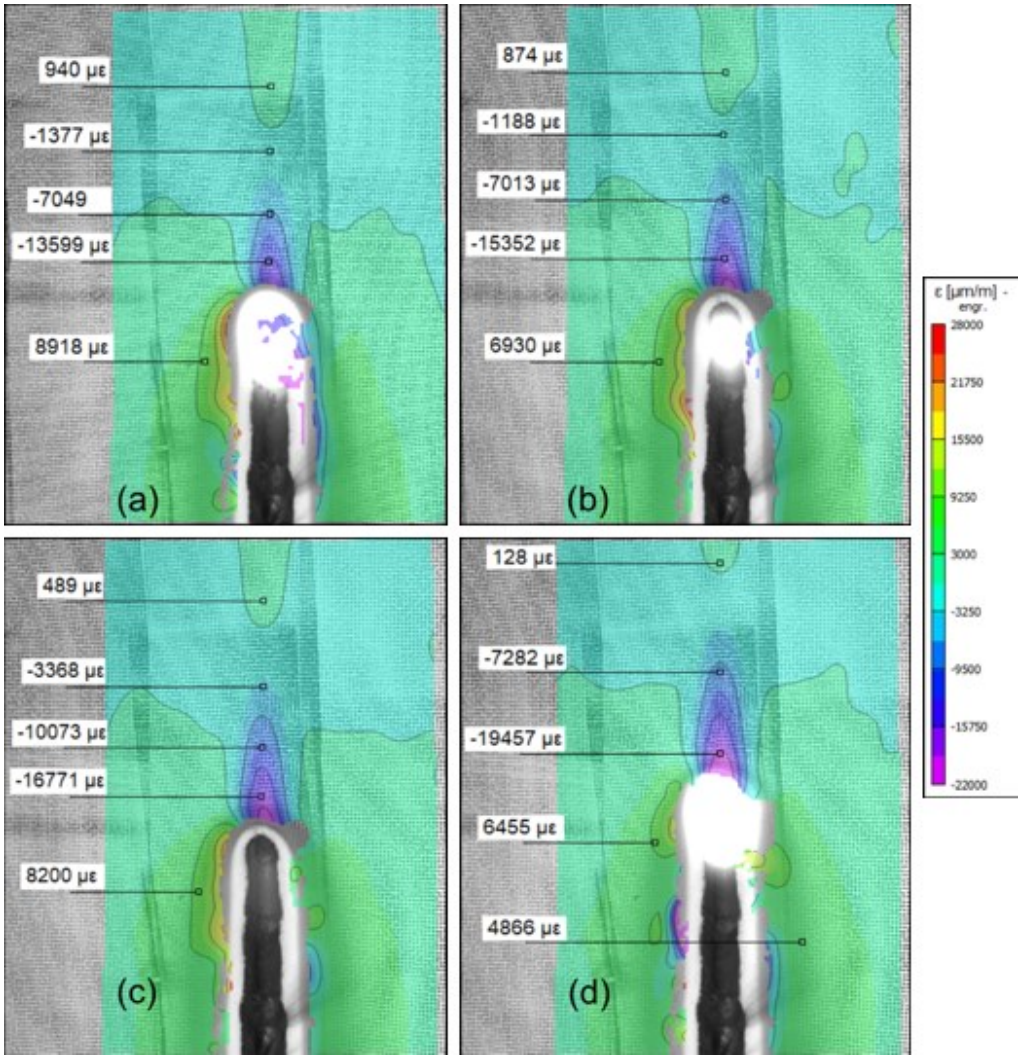

Fig. 14 Transversal strain measurement during the process of switching the filler rod: (a) prior to switching off the weld torch, (b) while the weld torch is fully switched off, (c) liquid weld pool on the back side of the plate, (d) weld torch back on.

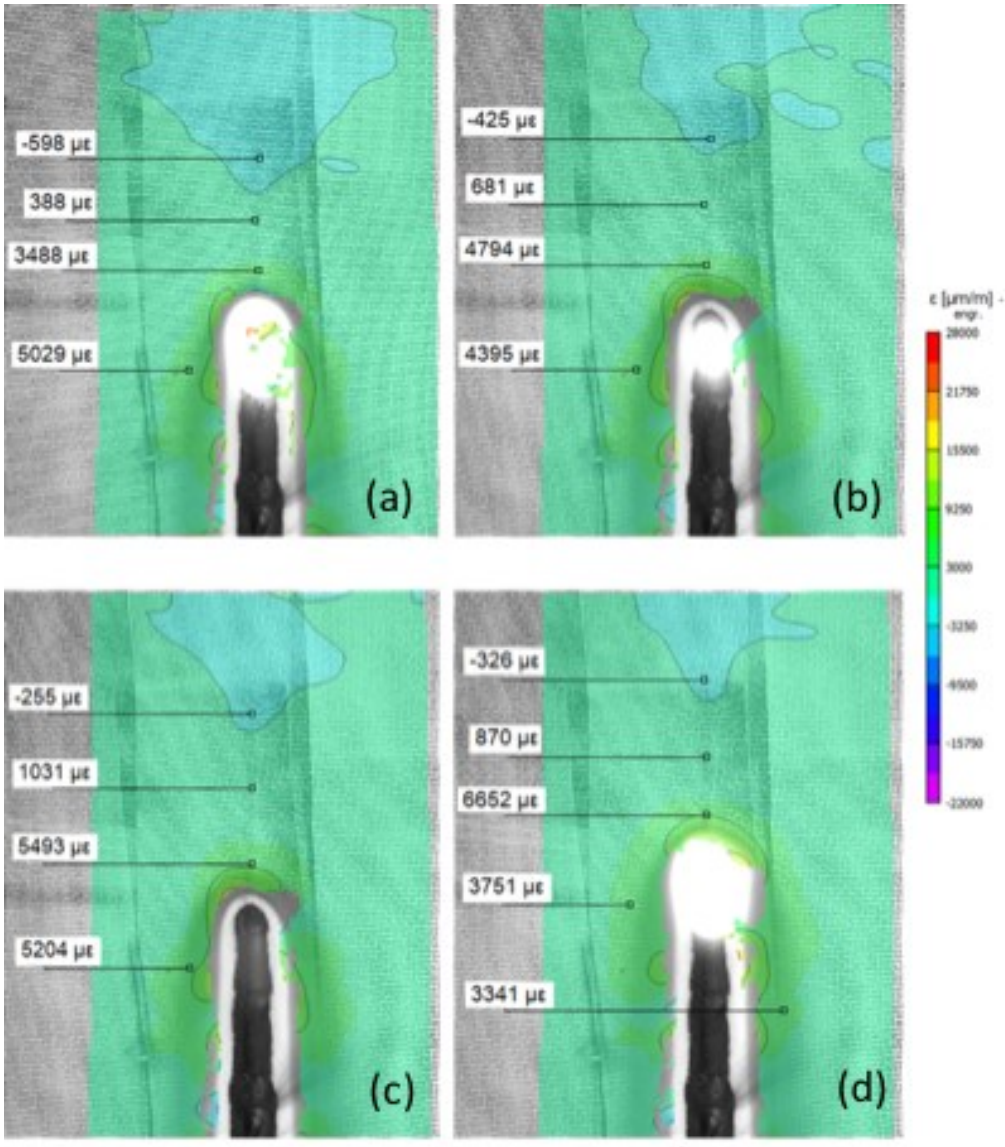

Fig. 15 Longitudinal (y-axis) strain readings during the process of switching the filler rod: a) right before switching the weld torch off, b) weld torch switched off, c) liquid weld pool solidified on the back side, d) weld torch back on.

A one to one comparison of transversal and or longitudinal strains of the experimental data set and the VrWeld model are presented in Fig. 16 and Fig. 17. The left image Fig. 16 shows the experimental transversal strain along the back of the plate. The right image shows the equivalent transversal strain results computed by the VrWeld model. The experimental data does not show data at the core of the weld pool, as in these locations the DIC speckle pattern is fully burned through. The results are shown for three-time steps, after, before and at time step for which the weld pool passes through. It is interesting to observe that the

change in transverse strain away from the weld pool is consistent with that of the VrWeld model. Variation and lack of symmetry in the experimental data are believed to be attributed to the changes in the weaving pattern of the welder and the inability of the DIC to compute strain in the proximity of the weld pool. The uncertainty in the peaks in the experimental data on either side of flat blue line for zero strain is high because the high temperatures from the weld pool destroyed the speckle pattern. Thus, DIC is computing the peaks with incomplete speckle patterns.

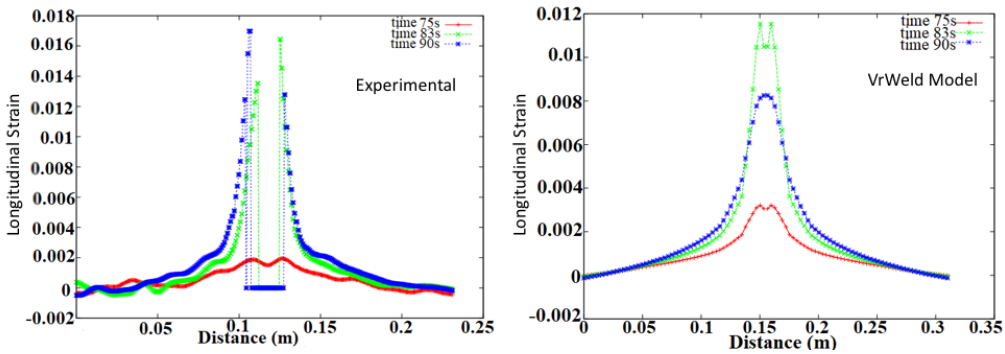

Fig. 16 Transversal strain comparison between the experimental (left) and VrWeld model (right) at 75, 83 and 90 seconds along a line y=7.5mm from the bottom edge of the plate.

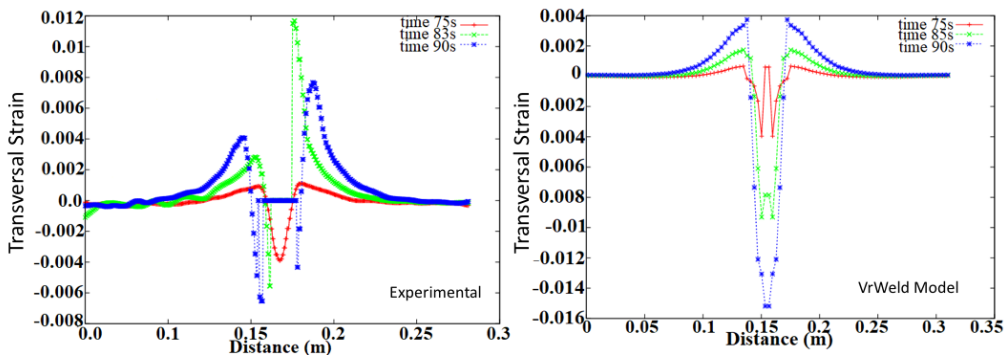

Fig. 17 Longitudinal strain comparison between the experimental (left) and VrWeld model (right) at 75, 83 and 90 seconds along a line y=7.5mm from the bottom edge of the plate.

Fig. 17 shows the experimental and VrWeld longitudinal strain along the transvers direction on the back of the plate. The left figure shows the experimental results while the right image shows the virtual data of the computed longitudinal strain distribution. Both experimental and VrWeld longitudinal strains show very good agreement. The longitudinal strain has less variations translating into a more symmetrical distribution of strain along the 3 different time steps.

COMPUTING TIMES AND USER TIMES

The computing times for these analyses using a single core Intel I7 processor with an Nvidia GPU for the weld pool model was 325 seconds with 36K 8-node brick FEM elements; VrWeld thermal analysis with 16,400 FEM elements took 319 seconds; 730 seconds for VrWeld stress solver 16,400 FEM elements. None of the correlations between real and virtual data took more than 2000 seconds. In contrast the DIC data file size was 24.4 Gb. The fiber data file size was 1.09 Gb.

SUMMARY AND CONCLUSIONS

Experimental data from a single pass GTIG manual weld in an A36 steel plate was gathered from four types of sensors, thermographic camera, fiber optic with Rayleigh back scattering, DIC displacement and strain sensors and voltage-current. This experimental data has been correlated with a 3D transient parametric computer model, VrWeld, that computes transient 3D temperature, microstructure, displacement, strain and stress. Both the experimental data and the virtual data have limited resolution in space and time and both have errors with respect to some expected ground truth for the real weld. In the authors' opinion, the correlation shows that the computer model has the potential to provide useful predictions for the design and optimization of welds and welded structures.

The most important lesson learned in this study is that as the accuracy, spatial resolution and temporal resolution of the sensor systems and the computer model increase, it becomes ever more important to synchronize the real and virtual clocks and the real and virtual spatial coordinate systems. The clock of each sensor system should not be set to zero at the start of an experiment. The clock of each sensor system should be set to Greenwich Mean Time. Also each sensor for spatial data should have fiducial marks that enable to the spatial coordinate system to computed for each set of spatial data.

The methods that were developed for synchronizing the real and virtual clocks and particularly the coordinate frames have been described. This is an essential part of correlating real and virtual data. In this study, the various sensor data systems had separate clocks. A data acquisition sensor that synchronized all sensor clocks in real time would be an improvement.

For example, adding at least four infrared LEDs fixed to the plate that could be captured by the thermographic camera is one possibility. The thermographic camera was hand held. A camera fixed in space would reduce camera motion. Although a thermographic camera that could record temperatures above 400°C would provide additional data, we were pleasantly surprised by the data this camera provided. Since the area of the 300°C isotherm was 10 mm^2 while the total area of the plate was $9x10^4$ mm^2 (300 mm by 300 mm), as such the area not sampled by the FLIR camera represents less than 0.01% ($10/9x10^4$) of the total area of the plate, Thus, 99.99% of the plate was sampled by the FLIR camera. Because the fields for temperatures below 400°C are very smooth and have low frequency modes, it is not essential to have a high-resolution camera. We could fit a polynomial to virtual

temperatures below 400°C. We would expect that the polynomial would be a low degree polynomial.

For each real thermal sensor, a set of 9 virtual thermal sensor's in the pattern of a 9-node quadrilateral FEM element and the centroid of the pattern the position specified for the real thermal sensor could be made. The quad edge length could be chosen to approximate the probable error in the position of the real thermal sensor. Then at a later stage of synchronizing real and virtual thermal sensors, one could choose the virtual real thermal sensor in the pattern that best matched the data for the real thermal sensor or interpolate data in the virtual pattern to estimate error in the position of the real thermocouple.

A global optimal design of experiment algorithm has been used with various objective functions that measure the difference between real and virtual data to optimize some of the parameters in the computer model for a parametric design space. To the author's knowledge, our demonstration of the correlation of transient space-time data from four sensor systems with a 3D parametric computer model of the weld is novel. In other research areas this might be called Data Fusion or Data Analytics, Deep Learning or artificial neural networks. They are all based on standard mathematics of statistics.

To the author's knowledge, this is the first demonstration of a local 3D transient Eulerian Ohjii-Sudnik weld pool model that is coupled with a microstructure solver. To the author's knowledge, this is the first publication of a 3D transient weld pool model that supports weave weld patterns. The solver for this weld pool model was then coupled with Lagrangian thermal and stress global solvers to compute transient 3D temperature, microstructure, displacement, stress and strain fields. As part of future work, we plan a detailed correlation between real and virtual microstructure evolution. It would be useful to use computer vision to measure the transient 3D geometry of the weld pool surface. This would enable one to define objective functions to optimize the design parameters for this weld pool model such as surface tension and arc pressure distribution.

The challenge of working with a manual weld is that the local weld speed, and transverse oscillations of the arc as a function of time are not known. Nevertheless, from both thermographic data and the DIC data, it was possible to estimate the actual local weld speed as a function of time. The uncertainty in the local weld speed would be expected to be less of a problem with welds made with a robot. However, because it is the reality of manual welds and because manual welds are an important welding technology it is important to study manual welds.

While [7] focusses on verification and validation of the computer models in computation weld mechanics, this study suggests that it is equally important to assess the accuracy of experimental data.

R.D. Rasch et al. in [8] wrote "Optimal research design implies that the objective of the investigation is determined in detail before the experiment or survey is carried out and that the precision requirements for the type of analysis planned for the data using the chosen statistical model are formulated and that all possible things which would have a negative

influence on the research work or could bias or disturb the results are considered. This all makes work, takes time, and is much more difficult than simply starting with the practical investigation and formulating the objective of the study after the data have been collected and then seeing the reliability the results have. Another reason that design methods are not used as much as they could or should be is that the designs are spread throughout a huge number of articles and books and they are sometimes not easy for the experimenter to understand."

The authors did not achieve this goal, but we did make progress toward this goal.

REFERENCES

[1] Website: *www.lunainc.com*, last accessed July 18-2018.

[2] Website: *www.correlatedsolutions.com*, last accessed July 18-2018.

[3] T. OHJI, T. MATSUTANI, F. MIYASKA and Y. HIRATA, *A mathematical model for circumferential GTA welding of pipe*, IIW Doc. 212-892-96.

[4] W. SUDNIK, D. RADAJ, W. EROFREW, *Validation of computerized simulation of welding processes, Mathematical Modelling of Weld Phenomena 4*, Editors H. Cerjak, H. K. D. H. Bhadeshia,

[5] J. A. GOLDAK, A. CHAKRAVARTI and M. J. BIBBY, *A New Finite Element Model for Welding Heat Sources, Trans. AIME*., Vol. 15B, June 1984, pp. 299-305.

[6] JONES, D.R., SCHONLAU, M. AND WELCH W.J. (1998). *Efficient global optimization of expensive black-box functions. Journal of Global Optimization*, 13, 455492.

[7] *Guide for Verification and Validation in Computation Weld Mechanics 1st Edition*, AWS A9.5:2013 An American National Standard Approved by the American National Standards Institute October 30, 2012.

[8] R.D. RASCH, J. PILZ, R VERDOOREN, A. GEBHARDT, *Optimal Experimental Design with R, Chapman and Hall*, 2011.